The Cylindrical Riemann Problem in Magnetohydrodynamics: A Case Study

W. Mostert[1]**, V. Wheatley**[1]**, M. Hingee**[1] **and R. Samtaney**[2]

[1]School of Mechanical and Mining Engineering
University of Queensland, Queensland 4072, Australia

[2]Mechanical Engineering
King Abdullah University of Science and Technology, Thuwal, Saudi Arabia

Abstract

A significant problem in inertial confinement fusion is that the material interfaces in the converging flow are subject to the Richtmyer-Meshkov instability when they are impulsively accelerated. It has been demonstrated that this instability can be suppressed in magnetohydrodynamic (MHD) flows at least for flow configurations with rectangular geometry. In order to understand the flow induced by attempting such suppression in converging flow configurations, it is necessary first to investigate the underlying base-flows, the canonical versions of which correspond to converging cylindrical and spherical MHD Riemann problems. Here, we present the numerical solution to one such case: the cylindrical MHD Riemann problem shown below with a uniform initial magnetic field of strength $\beta = 2$ and a pressure ratio of three across the interface. The wave structure is initially characterised by two outward- and two inward-moving waves, but as the solution develops, discontinuities form along the waves, producing a more complex flow structure. We investigate the different flow structures, their formation times, and identify how the compression achieved at the centre of the implosion is affected by the magnetic field.

Introduction

Inertial confinement fusion (ICF) is a process by which a capsule filled with a fuel such as deuterium or tritium is made to ablate rapidly by a spherical arrangement of incident radiation, sending a spherical shock into the centre of the capsule, aiming to compress the fuel to initiate a nuclear fusion burn. The effectiveness of ICF is limited to some degree by the Richtmyer-Meshkov instablity (RMI) [11, 15], which occurs when a shock wave interacts with a perturbed interface between fluids of different densities. The RMI is also relevant in areas such as astrophysics [1], supersonic and hypersonic airbreathing engines [19], reflected shock tunnels [18, 2], and shock-flame interactions [8].

In the case of ICF and astrophysical processes, the media in which the RMI occurs may be modelled as a plasma, and can therefore interact with applied and ambient magnetic fields. Furthermore, it has been demonstrated through numerical simulation [16, 22], shock theory [21] and linear analysis [20] that the RMI is suppressed in certain flow configurations, and it is well-known [4] that the Rayleigh-Taylor instability is suppressed at high wavenumbers under the same conditions.

In ICF, the RMI and Rayleigh-Taylor instabilities must be controlled to prevent the breakup of the target shell and successfully compress the fuel. As the target materials become rapidly ionized, the possibility exists of mitigating the RMI through the application of a magnetic field. However, while the converging shock driven hydrodynamic (HD) RMI has been investigated thoroughly in recent times [7, 13, 10], the equivalent MHD case with a magnetic field present has yet to be explored.

This study is intended as the first step in understanding the effect

of the magnetic field on the RMI in the cylindrically converging MHD case. While not investigating the RMI directly, it involves simulation, analysis, and interpretation of the cylindrical, two-dimensional (2D) MHD Riemann problem with applied magnetic field as shown in Figure 1, as a canonical flow. This corresponds to base-flow that will underlie later MHD RMI simulations. As such, understanding this flow is critical to analysis and interpreting future simulations where the RMI is present. The laterally applied magnetic field configuration is used since it is the most basic, and yet shows a rich resultant flow structure, as can be seen in Figure 2.

This paper begins with a qualitative discussion on the structure of the solution, where major features of the flow are identified. This is followed by an analysis of the early-time behaviour of the flow, enabling identification of the types of observed waves. Features of the 2D flow at intermediate and late times are then examined and explained, and finally, the point of convergence is compared with the HD (zero magnetic field) case.
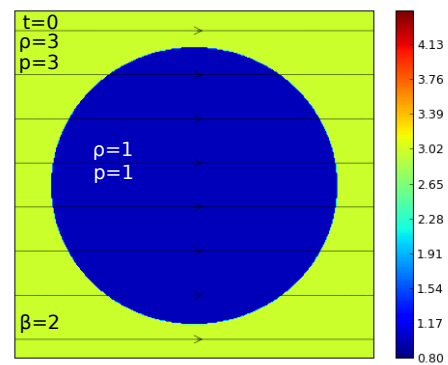

Figure 1: Initial configuration of the cylindrical MHD Riemann problem ($t = 0$). Magnetic field lines are overlaid. All quantities non-dimensional, with time normalized by the Alfvén time.
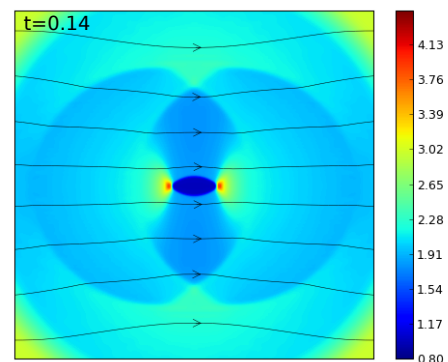

Figure 2: Developed pressure distribution at $t = 0.14$.

Formulation

The set-up for the 2D-cylindrical converging Riemann problem is shown in Figure 1, with overlaid magnetic field lines indicating field strength and direction. It consists of two uniform quiescent fluids separated by a circular interface. Since the high pressure region is surrounding the low pressure region, the resultant flow will converge. Across the interface, the pressure and density ratios are $\frac{p}{p_0} = \frac{\rho}{\rho_0} = 3$, where p_0 and ρ_0 are the non-dimensional base pressure and density, respectively. All variables are non-dimensional and base variables are defined as occurring on the inner side of the interface. A uniform magnetic field $\mathbf{B} = B_0 \hat{\mathbf{e}}_\mathbf{x}$ with non-dimensional strength $\beta = \frac{2p_0}{B_0^2} = 2$ is applied in the x-direction across the system. The fluid has a specific heat ratio $\gamma = \frac{5}{3}$. The model is ideal and neglects diffusion effects, which occur over a much larger timescale than advection effects. We define θ as the angle from the positive x-axis.

The numerical method uses compressible ideal MHD equations using an unsplit upwinding method containing an eight-wave upwinding formulation, of the sort described in Samtaney [16, 17, 5]. The magnetic field is kept divergence-free with the projection method [17]. The grid used in this analysis is a uniform cartesian 800-square mesh over non-dimensional length variables x and y varying from -1 to 1. The initial interface is centred at the origin and has radius $r = 0.3$.

Overall solution structure

The wave structure can be seen in Figure 3, which shows the distribution of the vorticity and density gradient at various times. Vorticity is shown as it clearly shows the locations of most of the MHD waves, while the density gradient shows the location of the density interface, which is prohibited from carrying shear by the MHD Rankine-Hugoniot relations. The early time flow strucure consists of two inward-moving and two outward-moving waves bracketing the contact. The outermost expansion is not visible in vorticity, but its presence can be deduced in the $t = 0.04$, $t = 0.08$, and $t = 0.12$, plots where the magnetic field lines outside the visible wave structure are made to bend from their initial horizontal orientation, showing the two-way coupling between the fluid motion and the magnetic field.

All waves originate from the interface, and are therefore initially circular; the increasing aspect ratio depends on the wave speeds on magnetic field orientation. At $t = 0.12$ singularities in the wave curvature ("kinks") develop at $\theta = \pm 90°$ in the slower converging wave; as this kink moves inward, other kinks bracketing $\theta = \pm 90°$ in the diverging wave also appear. Also visible is a flattening of the innermost wave at $t = 0.12$, so that, at $\theta = \pm 90°$ the wave converges at a different rate than at $\theta = 0°, 180°$. This behaviour is inverted in the slower converging wave, which approaches the centre more quickly at $\theta = 0°, 180°$ than at $\theta = \pm 90°$. All waves approach zero vorticity at $\theta = 0°, 180°$, and $\pm 90°$.

Early-time wave structure

At very early times, the wave structure in the radial direction at any point along the interface can be estimated from the solution to the one-dimensional (1D) planar Riemann problem with the local magnetic field orientation, as curvature effects are initially small. Thus, to understand the flow further, we observe the pressure, density, and vorticity developments along radial lines and compare these to the 1D equivalents. A combined plot showing such a comparison between the 1D and 2D solutions at certain angles to the magnetic field is shown in Figure 4.
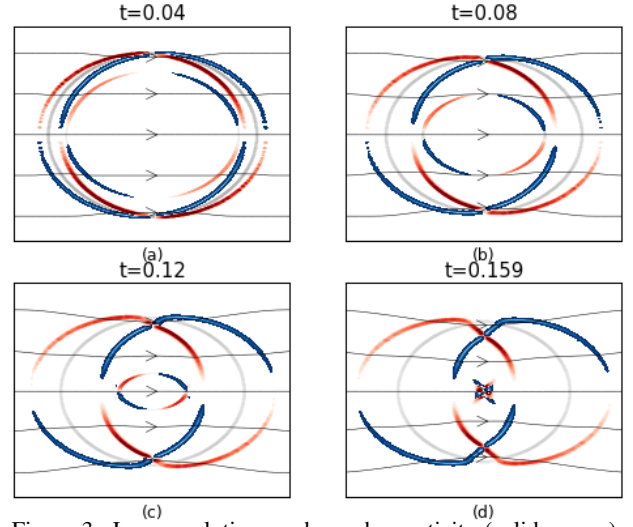

Figure 3: Jump evolution as shown by vorticity (solid curves) overlaid on density gradient (faint pseudo-circular structure). Vorticity shows the jumps of interest; density gradient shows the contact surface.
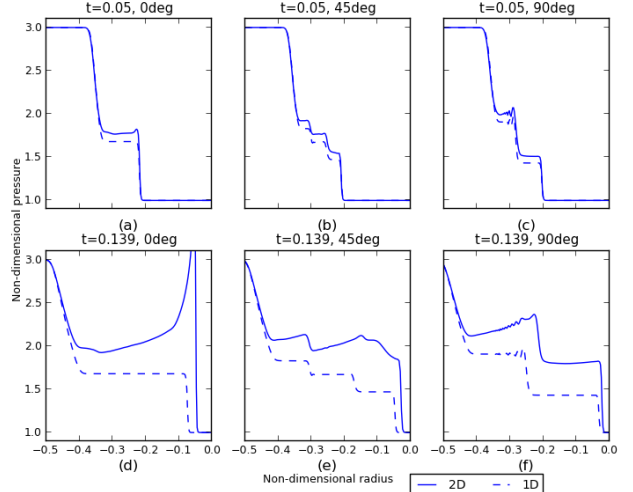

Figure 4: Comparison of non-dimensional pressure in the 1D and cylindrical 2D Riemann problems along rays at selected angles to the magnetic field. Stippled lines indicate the quasi-1D result and solid lines indicate the 2D result.

The 1D solutions are formulated under the same pressure and density ratios and β-value as in the 2D case, with the applied magnetic field at the same angle to the interface as it is along the ray of interest. Figure 4 shows that, at early times, there is excellent correlation between the 1D and 2D cases for both jump strength and speed.

The outward-moving waves move at the same speed for both cases, indicating that they are MHD expansions moving at the fast and slow magnetosonic speeds. The inward-moving waves increase in velocity relative to the 1D case, implying that they are magneto-sonic shocks, accelerating due to shock focussing.

Using the usual classification system [6], the waves in the 1D case are tracked and classified. The following observations are made:

- At $\theta = 0°$, the HD case is observed, with an inward-travelling shock and an outward-travelling expansion.

- For $0° < \theta < 90°$, four jumps (not counting the contact surface) are seen: an outward-travelling fast expansion, a (generally) outward-travelling slow expansion, an inward-travelling slow shock, and an inward-travelling fast shock. For higher $\theta > 60°$ the slow expansion appears to be

slowly *inward-travelling*, though the flow over it is still left-to-right. The slow magneto-sonic speeds decreases at higher θ, leading to the slow expansion and shock moving more slowly.

- At θ = 90°, the slow expansion and shock never separate from the contact surface. Analysis indicates that total pressure $\frac{1}{2}p_0^2 + |B|^2$ remains constant across this "combined" jump, allowing its classification as a *tangential discontinuity*.

Some numerical oscillations are visible in the θ = 90° case, due to our use of a low-dissipation Riemann solver. The resolution that was used was sufficient to resolve all features of the flow. As we are simulating equations with no physical dissipation to set a minimum length-scale, pointwise grid convergence is not a relevant concept.

We now translate this information to the 2D case in order to interpret the shock structure.

Details at intermediate times

We assume that the fundamental nature of the shocks remain unchanged. Some special features of the two-dimensional flow will now be discussed in light of the (now known) wave types.
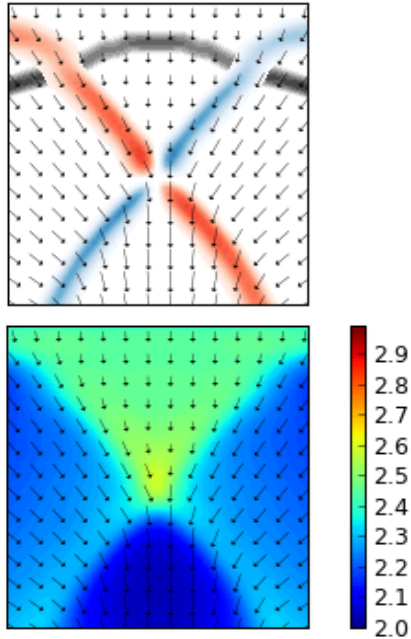

Figure 5: Closeup view of kink in converging slow shock and surrounding wave structure with superimposed velocity vector field at $t = 0.17$. Vorticity in red and blue and density gradient in grey. Pressure distribution shown for wave type identification.

Figure 3 shows a clear decrease of vorticity at θ = 0°, 180° and θ = ±90°. At 0° and 180°, this is because the shocks are hydrodynamic and have zero jump in tangential velocity across them, so they do not carry vorticity. At ±90°, the vorticity must pass through zero due to the symmetry of the velocity field.

At θ = 0° and 180°, the slow and fast shocks travel together. Since the component of the magnetic field tangential to the shocks here is zero, the slow and fast shocks actually exist as a single HD shock. At later times, the fast shock moves away from the slow shock due to multidimensional effects. The same is true for the slow and fast expansions, though the latter of these is not visible in Figure 3.

The "kink" in the converging slow shock that forms around time $t = 0.08$ at angle θ = 90° is initially placed on the contact surface, where the 1D analysis predicts a tangential discontinuity. In the 2D case, this behaviour changes at later times. Figure 5 shows the neighbourhood of the kink at $t = 0.17$ with an overlaid velocity vector field; here, the kink has clearly moved inward from the contact surface.

Since the velocity field is horizontally converging near the kink, two additional refected waves form so that the horizontal components of the velocity field may be cancelled. Since these waves move inward and downward, Figure 5 shows that they are shocks, due to the upstream flow being at a lower pressure than downstream. These waves connect with the slow expansion wave structure away from θ = 90°, and form singularities in curvature at the connection points.

Late-time behaviour

Similar behaviour can be seen in the fast shocks at θ = 0° and 180°. Figure 6 shows the density distribution at the centre of the flow. (Density is more easily visualized than vorticity in this case.) Here, a kink forms at the slowest propagating point on the fast shock intersection. Similarly to at θ = 90°, this causes reflected waves to project outwards, away from the axis and meeting with the converging slow shocks nearby.
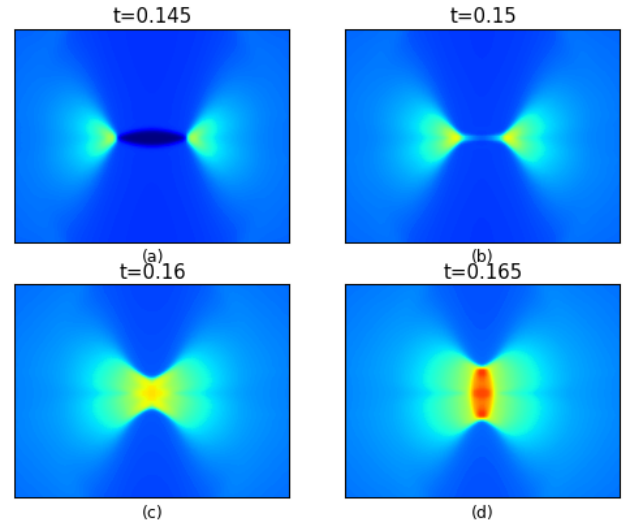

Figure 6: Closeup view of density distribution at the domain centre near convergence.
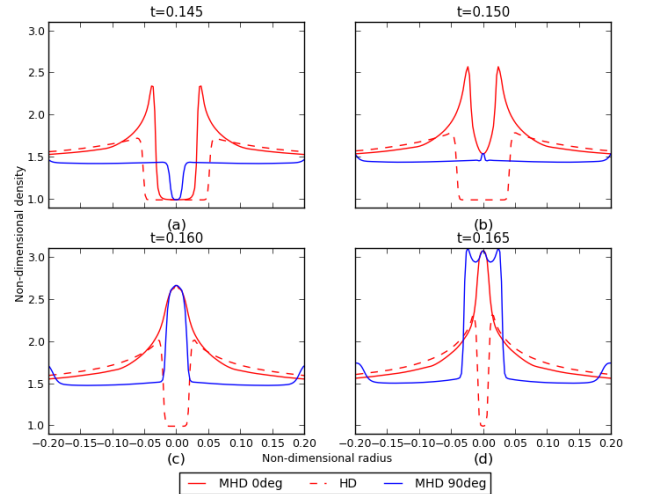

Figure 7: Profiles of the flow density for MHD and HD cases near the centre of domain. MHD cases are plotted at θ = 0°, 180° and θ = ±90°.

Figure 6 shows that the fast shock converges faster in the verti-

cal direction (along $\theta = \pm 90°$ than in the horizontal direction. This causes convergence in to occur in two stages. First the fast shocks are squeezed together from above and below, forming what appears to be a horizontal "line" of convergence in Figure 6(b); this is followed by the reflected shocks emanating from the fast shock kinks converging horizontally. The maximum density and pressure in the solution are generated at this time. This is in sharp contrast to the HD case, which is rotationally symmetric and convergence occurs at a point at a distinct time.

Figure 7 shows profiles of the MHD flow density at the same elapsed times as Figure 6 at angles of $\theta = 0°$ and $\pm 90°$, and compares these with the profile of the (rotationally symmetric) HD flow density at the same times. Convergence of the $\theta = \pm 90°$ shocks occurs first, as observed previously, at $t = 0.150$. The $\pm 90°$ density then peaks and diverging waves are visible, travelling outwards between $t = 0.160$ and $t = 0.165$. Convergence of the $\theta = 0°$ and $180°$ shocks follows at $t = 0.160$, beginning to form the diverging waves at $t = 0.165$. The HD shock converges last, after $t = 0.165$. The slightly faster convergence of the $\theta = 0°$ MHD shock compared to the HD shock is likely due to the formation of a kink at that angle, which propagates faster than the original smoothly curved shock.

The peak non-dimensional pressure and density experienced by the MHD flow are around 6.9 and 3.1 respectively, compared to the much higher HD peaks of 21.4 and 5.5 respectively. The significantly lower values in the MHD case are due to the increased area over which convergence occurs and the different behaviour of the horizontal and vertical flows. The width of the horizontal "line" of convergence is likely a function of the field strength and direction, the interface pressure ratio and initial radius, and some fluid properties; however, a parametric study of this feature is not included here.

Conclusions

This investigation considered the 2D cylindrical Riemann problem in MHD as a canonical flow. The flow structure was simulated numerically and compared with solutions to the 1D Riemann problems, leading to the classification of shocks and expansions in the flow. Additional structures in the flow due to multidimensional effects were also presented and discussed. The understanding gained from this case study will lead to better understanding of other canonical MHD flows and pave the way for analysis of MHD RMI behaviour in converging flows.

Acknowledgements

References

[1] Arnett D. The role of mixing in astrophysics. *Ap. J. Suppl.*, **127**, 2000, 213-217.

[2] Brouillete M. The Richtmyer-Meshkov instability. *Ann. Rev. Fluid Mech.*, **34**, 2002, 445-468.

[3] Cao J.T., Hu Z.W., Ren H.J., and Li. D. Effects of shear flow and transverse magnetic field on Richtmyer-Meshkov instability. *Phys. Plasmas*, **15**, 2008.

[4] Chandrasekhar S. *Hydrodynamic and hydromagnetic stability*. Oxford University Press, 1961.

[5] Colella P., Multidimensional upwind methods for hyperbolic conservation laws, *J. Comput. Phys.*, **87**, 1990, 171.

[6] Goedbloed J.P., Keppens R., and Poedts S. *Advanced Magnetohydrodynamics*. Cambridge University Press, 2010, 505.

[7] Hosseini S.H.R. and Takayama K. Experimental study of Richtmyer-Meshkov instability induced by cylindrical shock waves. *Phys. Fluids*, **17**, 2005, 084101.

[8] Khoklov A.M., Oran E.S., and Thomas G.O. Numerical simulation of deflagration to detonation transition: the role of shock-flame interactions in turbulent flames. *Combust. Flames*, **117**, 1999, 323-339.

[9] Lindl J.D., McCrory R.L., and Campbell E.M. Progress toward ignition and burn propagation in inertial confinement fusion. *Physics Today*, **45**, 1992, 32-40.

[10] Lombardini M. and Pullin D.I. Small-amplitude perturbations in the three-dimensional cylindrical Richtmyer-Meshkov instability. *Phys. Fluids*, **21**, 2009, 114103.

[11] Markstein G.H. Flow disturbances induced near a slightly wavy contact surface, or flame front, traversed by a shock wave. *J. Aero. Sci.*, **24**, 1957, 238-239.

[12] Meshkov E.E. Instability of the interface of two gases accelerated by a shock wave. *Sov. Fluid Dyn.*, **4**, 1969, 101-108.

[13] Mikaelian K.O. Rayleigh-Taylor and Richtmyer-Meshkov instabilities and mixing in stratified cylindrical shells. *Phys. Fluids*, **7**, 2005, 094105.

[14] Powell K.G., Roe P.L., Linde T.J., Gombosi T.I., and DeZeeuw D.L. A solution adaptive upwind scheme for ideal magnetohydrodynamcs. *J. Comp. Phys.*, **154**, 1999, 284-309.

[15] Richtmyer R.D. Taylor instability in shock acceleration of compressible fluids. *Comm. Pure and Appl. Math.*, **13**, 1960, 297-319.

[16] Samtaney R. Suppression of the Richtmyer-Meshkov instability in the presence of a magnetic field. *Physics of Fluids*, **15(8)**, 2003, L53-L56.

[17] Samtaney R., Colella P., Ligocki T.J., Martin D.F., and Jardin S.C. An Adaptive mesh semi-implicit conservative unsplit method for resistive MHD. *Journal of Physics: Conference Series*, **16**, 2005, 40-48.

[18] Stalker R.J. and Crane K.C.A. Driver gas contamination in a high-enthalpy reflected shock-tunnel. *AIAA J.*, **16**, 1978, 277-279.

[19] Yang J., Kubota T., Zukoski E.E. Applications of shock induced mixing to supersonic combustion. *AIAA J.*, **31**, 1993, 854-862.

[20] Wheatley V., Pullin D.I., and Samtaney R. Stability of an Impulsively Accelerated Density Interface in Magnetohydrodynamics. *Phys. Rev. Lett.*, **95**, 2005, 125002.

[21] Wheatley V., Pullin D.I., and Samtaney R. Regular shock refraction at an oblique planar density interface in magnetohydrodynamics. *J. Fluid Mech.*, **522**, 2005, 179-214.

[22] Wheatley V., Samtaney R., and Pullin D.I. The Richtmyer-Meshkov instability in magnetohydrodynamics. *Phys. Fluids*, **21**, 2009, 082102.